Journal of ELECTRONIC MATERIALS, Vol. 45, No. 10, 2016
DOI: 10.1007/s11664-016-4694-z
© 2016 The Minerals, Metals & Materials Society

CrossMark

Effect of Oxidation Temperature on Physical and Electrical Properties of Sm_2O_3 Thin-Film Gate Oxide on Si Substrate

KIAN HENG GOH,[1] A.S.M.A. HASEEB,[1] and YEW HOONG WONG[1,2]

1.—Department of Mechanical Engineering, Faculty of Engineering, University of Malaya, 50603 Kuala Lumpur, Malaysia. 2.—e-mail: yhwong@um.edu.my

Thermal oxidation of 150-nm sputtered pure samarium metal film on silicon substrate has been carried out in oxygen ambient at various temperatures (600°C to 900°C) for 15 min and the effect of the oxidation temperature on the structural, chemical, and electrical properties of the resulting Sm_2O_3 layers investigated. The crystallinity of the Sm_2O_3 films and the existence of an interfacial layer were evaluated by x-ray diffraction (XRD) analysis, Fourier-transform infrared (FTIR) spectroscopy, and Raman analysis. The crystallite size and microstrain of Sm_2O_3 were estimated by Williamson–Hall (W–H) plot analysis, with comparison of the former with the crystallite size of Sm_2O_3 as calculated using the Scherrer equation. High-resolution transmission electron microscopy (HRTEM) with energy-dispersive x-ray (EDX) spectroscopy analysis was carried out to investigate the cross-sectional morphology and chemical distribution of selected regions. The activation energy or growth rate of each stacked layer was calculated from Arrhenius plots. The surface roughness and topography of the Sm_2O_3 layers were examined by atomic force microscopy (AFM) analysis. A physical model based on semipolycrystalline nature of the interfacial layer is suggested and explained. Results supporting such a model were obtained by FTIR, XRD, Raman, EDX, and HRTEM analyses. Electrical characterization revealed that oxidation temperature at 700°C yielded the highest breakdown voltage, lowest leakage current density, and highest barrier height value.

Key words: Samarium oxide, oxidation, sputtering, stoichiometry

INTRODUCTION

Nowadays, electronic devices require superior characteristics and performance such as high speed, low cost, small size, high reliability, high package density, and low power consumption due to rapid developments in the semiconductor industry.[1–4] During the last few decades, silicon dioxide (SiO_2) has been widely used as a gate oxide layer on silicon substrates in the microelectronics industry because of its excellent insulating properties and formation of good native oxide. However, physically thicker layers but with the same electrical equivalent thickness will be required for future nanoscale metal–oxide–semiconductor (MOS) technology.

(Received February 1, 2016; accepted May 21, 2016; published online June 22, 2016)

Many research studies have been carried out on replacement of SiO_2 gate oxide with HfO_2,[4,5] ZrO_2,[4–6] ZrON,[7–13] Al_2O_3,[4,6] La_2O_3,[4,14–16] TiO_2,[4,6,17–19] Ta_2O_5,[4,6,17–19] and Y_2O_3.[4,6] However, each of these has its own drawbacks compared with SiO_2. Recently, various rare-earth oxides (REOs) have been investigated due to their superior properties.[15,20,21] Samarium oxide (Sm_2O_3) is one of the promising candidate materials among such rare-earth oxides because of various outstanding properties such as high dielectric constant (7 to 15), high breakdown electric field (5 MV/cm to 7 MV/cm), large bandgap (4.33 eV), low leakage current, large conduction band offset with Si, good thermal stability, low frequency dispersion, and low trapping rates.[15,20,22–24] Sm_2O_3 is also predicted to be thermodynamically stable on Si substrate.[22] Moreover,

Sm_2O_3 is less hygroscopic among the REOs because of its smaller ionic radius and less electropositive properties.[25]

Various deposition methods and postannealing processes for oxides have been studied over the last 20 years. Sm_2O_3 films have been deposited by several methods such as atomic layer deposition,[15] metalorganic chemical vapor deposition (MOCVD),[26] pulsed layer deposition (PLD),[27] thermal evaporation,[28] vacuum evaporation,[29] resistive evaporation,[30] and direct-current (DC) and radiofrequency (RF) sputtering.[22–24,31,32] DC and RF sputtering deposition are usually followed by postdeposition annealing (PDA) at various temperatures in oxygen or nitrogen ambient.

For Sm_2O_3 films deposited by MOCVD, strong crystallization occurs with cubic phases formed at lower temperatures. With increasing deposition temperature, Sm_2O_3 with preferred (111) orientation and monoclinic structure is detected. The surface roughness decreases as the deposition temperature is increased.[26] Sm_2O_3 film deposited by RF reactive sputtering and annealed at 700°C exhibited the smoothest surface and best electrical results, among different annealing temperatures tested (600°C to 800°C).[22] An SiO_2 interfacial layer grows rapidly at 800°C due to oxygen diffusion from Sm_2O_3 to the Si substrate.[22] Sm_2O_3 films deposited by thermal evaporation remain amorphous even after PDA at up to 600°C.[28] Smooth and amorphous Sm_2O_3 film can be achieved by both PLD and RF-PLD at room temperature. Neither Sm silicate nor SiO_2 were detected between Sm_2O_3 and the Si substrate.[27] Polycrystalline Sm_2O_3 films are formed at room temperature in argon ambient by RF magnetron sputtering.[31] Among various PDA temperatures (100°C to 400°C), PDA at 200°C resulted in the smoothest surface and lowest leakage current due to lesser crystal defects.[23] Relatively high deposition and annealing temperatures and the metal ionic radius facilitated formation of a metal silicate interlayer.[33] The silicate interlayer will increase the equivalent oxide thickness, degrading the electrical properties.

Among the deposition techniques, MOCVD requires high temperature to decompose the metalorganic precursor compound, and the presence of carbon, chlorine, and hydrogen may degrade the electrical properties.[18,22] Molecular beam epitaxy (MBE) deposition may create positively charged defects due to low oxygen supply resulting from low oxygen partial pressure during deposition.[34] RF magnetron sputtering offers a high deposition rate, low substrate temperature rise, and good adhesion between the film and substrate.[35] Although straightforward RF cosputtering of a samarium target in mixed oxygen/argon ambient followed by PDA is an easier approach, it may oxidize the silicon substrate to form a thick SiO_2 interlayer during deposition.[36] A sputtering process with a pure metal target followed by thermal oxidation is preferable because the metal oxide film and interfacial layer can be controlled during the thermal oxidation process. Stoichiometric metal oxide film can be formed.[8,9,12] However, use of this method for formation of samarium oxide thin films has not yet been reported.

In this study, the effects of the oxidation temperature during the thermal oxidation process after sputtering with a pure samarium target were studied, since temperature plays a main role in the physical and electrical properties of the resulting thin films. Moreover, the growth mechanisms of Sm_2O_3 and the interfacial layer have not been fully investigated yet. As summarized in Table I, only one study analyzed the deposited film using transmission electron microscopy (TEM) analysis, whereas three studies analyzed the deposited layer using x-ray photoelectron spectroscopy (XPS) only. Hence, HRTEM analysis was carried out to reveal

Table I. Summary of thickness and its root-mean-square (RMS) variation, and interfacial layer characterization methods of Sm_2O_3 films deposited by various previous methods

No.	Deposition method	Thickness (nm)	RMS (nm)	Interfacial layer characterization method	Ref.
1	ALD	50	1.2	–	15
2	RF sputtering	7.5–8.2	0.19–0.37	XPS	22
3	DC sputtering	120	3.43–7.81	XPS	23
4	RF sputtering	25	–	XPS	24
5	MOCVD	120	3.9–7.9	–	26
6	PLD	61.4	5–10	SEM	27
7	Thermal evaporation	122.2	–	–	28
8	Vacuum evaporation	230–300	–	–	29
9	RF sputtering	61	–	TEM	31
10	RF sputtering	120	–	–	32
11	RF sputtering	110–125	5.2–19.5	–	52

ALD, atomic layer deposition.

the growth mechanisms of Sm_2O_3 and the interfacial layer. The physical and electrical properties of the Sm_2O_3 films with different oxidation temperatures are also discussed.

EXPERIMENTAL PROCEDURES

Silicon substrates [n-type, (100)-oriented, 1 Ω cm to 10 Ω cm, 1 cm × 1 cm] were cleaned by standard Radio Corporation of America (RCA) cleaning procedures followed by dipping for 15 s into hydrofluoric acid (HF) solution (1:50 HF:H_2O). Metallic Sm film with thickness of 150 nm was sputtered from a Sm target (Kurt J. Lesker, USA, 99.9% purity) using a TF 450 physical vapor deposition (PVD) radiofrequency (RF) sputtering system. The working pressure, RF power, and argon gas flow rate were regulated at 3×10^{-5} mbar, 170 W, and 25 cm^3/min, respectively. A Carbolite CTF tube furnace was heated up to a set of oxidation temperatures (600°C, 700°C, 800°C, and 900°C) with heating rate of 10°C/min and argon gas flow rate of 150 mL/min. Once the temperatures were achieved, samples of sputtered Sm on Si were placed into the tube furnace with oxygen flow rate of 150 mL/min for 15 min. The oxidized samples were then cooled down in the tube furnace before removal.

The properties of the samples were investigated by various characterizations methods. Film crystallinity was characterized using a PANalytical Empyrean x-ray diffractometer (XRD) system in the 2θ scan range from 20° to 90°. Copper radiation (Cu K_α) with wavelength (λ) of 0.15406 nm was used as x-ray source. Cross-sectioned film was analyzed by TECNAI G2 F20 high-resolution transmission electron microscope (HRTEM) after deposition of platinum (Pt) on the sample surface to protect it from ion bombardment damage caused by the focused ion beam during lamella preparation. The chemical composition of the samples was determined by energy-dispersive x-ray (EDX) analysis using an Oxford Instrument X-Max^N 80T SDD detector. The interplanar spacing (d) of the polycrystalline structure was measured from HRTEM images using ImageJ software, yielding measurement accuracy of three decimal places. A Veeco D3100 atomic force microscope (AFM) was used to analyze the surface topography and obtain the root-mean-square (RMS) value in noncontact mode on 1 μm × 1 μm scanned surface areas. Chemical functional groups of the films were analyzed using a PerkinElmer Spectrum 400 Fourier-transform infrared (FTIR) spectrometer. Chemical bonding stability measurements were carried out using a Horiba Xplora One Raman spectrometer.

MOS capacitor test structures with area of 3 μm × 3 μm were fabricated to investigate the electrical properties of the films. Aluminum (Al, 99.9995% purity, 100 nm; Kurt J. Lesker, USA) was sputtered through a mask using a TF 450 PVD RF sputtering system. The back side of the Si was also sputtered with 100-nm-thick Al film to form an Ohmic back contact. Current–voltage (I–V) measurements were conducted using a BPW-800 8″ probe station with a Keithley 4200 semiconductor characterization system (SCS).

RESULTS AND DISCUSSION

Figure 1 shows the XRD patterns of the Sm films sputtered on Si substrate after oxidation at different temperatures (600°C, 700°C, 800°C, and 900°C). Three strong peaks at 28°, 69°, and 76° were detected for all samples, matching three different planes of the cubic structure of silicon: c-Si (111), c-Si (004), and c-Si (331), respectively; these peaks are confirmed by Inorganic Crystal Structure Database (ICSD) with reference code 98-001-6569. The cubic structure of Sm_2O_3 (c-Sm_2O_3) was revealed at various diffraction angles of 17.8°, 19.9°, 38.6°, 46°, 48°, 54°, 56°, 58.5°, 61°, 74.7°, and 75.5°, corresponding to (002), (112), (233), (152), (334), (154), (226), (444), (064), (138), and (257) planes, respectively. These peaks are confirmed by ICSD with reference code 98-004-0475. According to the XRD results, it was observed that the peaks at 38.6°, 46° and 58.5° increased in intensity and became sharper as the oxidation temperature of the samples was increased from 600°C to 900°C, as shown in Fig. 2, implying that the crystallinity of Sm_2O_3 increased with the oxidation temperature.

Peak broadening in XRD patterns can also be used to evaluate the crystallite size (D) and microstrain (ε) due to crystal defects such as dislocations.[37] The crystallite size (D) and microstrain (ε) can be extracted using three methods: (1) the simplified integral breadth method, (2) the Fourier method, and (3) the double Voigt method. Of these three methods, the simplified integral breadth method gives an average value instead of a crystallite size

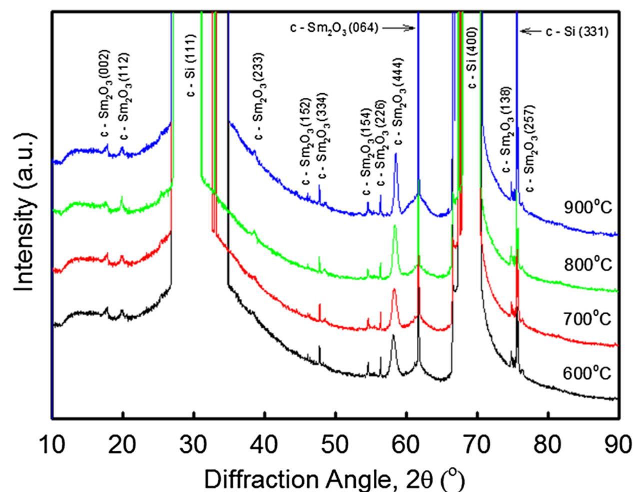

Fig. 1. XRD patterns of samples oxidized at various temperatures (600°C to 900°C).

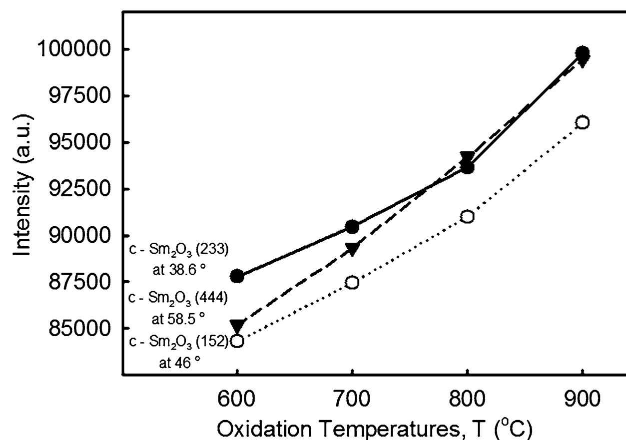

Fig. 2. Intensities of Sm_2O_3 (233), (444), and (152) peaks at 38.6°, 58.5°, and 46°, respectively, as functions of oxidation temperature (600°C to 900°C).

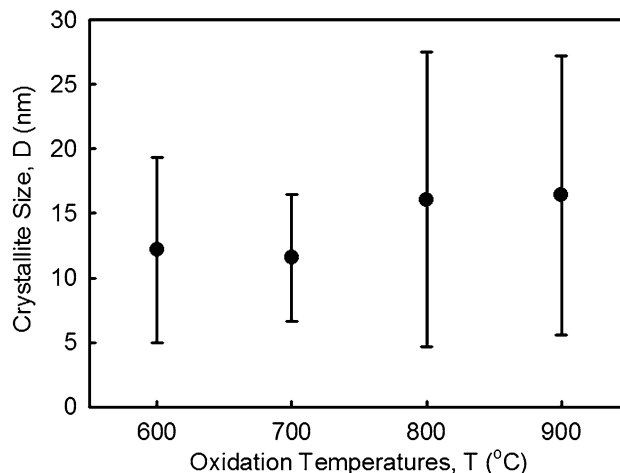

Fig. 3. Crystallite size calculated by Scherrer equation for Sm_2O_3 as function of oxidation temperature (600°C to 900°C).

distribution.[38–42] The simplified integral breadth method consists of two basic approaches: (1) Debye–Scherrer analysis, and (2) Williamson–Hall (W–H) analysis.[40,41]

In Debye–Scherrer analysis, the Scherrer equation is used to estimate the crystallite size D of Sm_2O_3[37,40] as

$$D = \frac{K\lambda}{\beta_{\mathrm{D}} \cos\theta} \tag{1}$$

where λ is the wavelength of the radiation; K is a constant, which is equal to 0.9; β_{D} is the peak width at half-maximum intensity; and θ is the peak position. Using the Scherrer equation, the average crystallite size of Sm_2O_3 samples with oxidation temperature of 600°C, 700°C, 800°C, and 900°C was calculated using various peaks to be 1.22 nm, 1.16 nm, 1.61 nm, and 1.64 nm, respectively (Fig. 3). Since the Scherrer equation only gives a lower bound on the crystallite size and microstrain is not take into account, W–H analysis was also conducted.[37]

Unlike Debye–Scherrer analysis, W–H analysis can analyze crystallite sizes at various 2θ positions at once, instead of only a single 2θ position. Apart from crystallite size, lattice strain is another, independent factor contributing to total peak broadening.[37,40,43] The strain-induced broadening due to crystal distortion and imperfections is given by

$$\varepsilon = \frac{\beta_{\mathrm{S}}}{4\tan\theta}, \tag{2}$$

where β_{S} is the peak width at half-maximum intensity and θ is the peak position. From Eqs. 1 and 2, it is clear that the peak width from strain varies as $\tan\theta$ (integral breadth of Gaussian component) whereas the crystallite size varies as $1/\cos\theta$ (integral breadth of Lorentzian component).[40,41,43] For W–H analysis, assuming that the crystallite size and strain contributions to the peak broadening are independent and both have a Cauchy-like profile (a convolution of a Gaussian and Lorentzian profile), the peak broadening is the sum of the Scherrer equation (Eq. 1) and strain-induced broadening (Eq. 2):[37,40,41,43,44]

$$\beta_{hkl} = \beta_{\mathrm{D}} + \beta_{\mathrm{S}} \tag{3}$$

$$\beta_{hkl} = \frac{K\lambda}{\beta_{\mathrm{D}} \cos\theta} + 4\varepsilon\tan\theta. \tag{4}$$

Rearranging, the W–H equation becomes

$$\beta_{hkl}\cos\theta = \frac{K\lambda}{D} + 4\varepsilon\sin\theta. \tag{5}$$

Based on Eq. 5, one plots a graph of $\beta_{hkl}\cos\theta$ versus $4\sin\theta$ (Fig. 4). Five points with the best goodness of fit (r^2) are selected from the distribution of values. ε is the gradient while $K\lambda/D$ is the intercept of the graph, from which D can be calculated. Based on W–H analysis, the crystallite size of Sm_2O_3 increased from 9.32 nm to 65.77 nm as the microstrain of Sm_2O_3 increased from 0.033 to 0.060 as the oxidation temperature was increased from 600°C to 900°C (Fig. 5). The crystallite sizes of Sm_2O_3 calculated by both the Scherrer equation and W–H analysis exhibit the same trend with increasing oxidation temperature.

FTIR analysis was used to determine the chemical functional groups in the samples. Figure 6 shows the FTIR transmittance spectra (700 cm^{-1} to 400 cm^{-1}) for the samples of Sm sputtered on Si substrates for the different oxidation temperatures. The Si–Si vibration mode band was located at 567 cm^{-1} for all samples, broadening as the oxidation temperature was increased. For oxidation temperature of 600°C, Sm–O vibration modes were detected at 409 cm^{-1},[45] 418 cm^{-1},[45,46] 432 cm^{-1},[45,47]

Fig. 4. W–H plot of samples oxidized at various temperatures (600°C to 900°C).

Fig. 5. Crystallite size and microstrain calculated from W–H plot as functions of oxidation temperature (600°C to 900°C).

439 cm^{-1},[45,47] 459 cm^{-1},[45,48] 473 cm^{-1},[46,48] 482 cm^{-1},[45,46] and 502 cm^{-1}.[45] However, these peaks shifted or broadened as the oxidation temperature was further increased to 700°C, 800°C, and 900°C. The peaks for the 700°C, 800°C, and 900°C samples at 482 cm^{-1} and 502 cm^{-1} broadened as the temperature was increased. All the peaks at 473 cm^{-1} broadened and decreased in intensity as the oxidation temperature was increased. The peak at 459 cm^{-1} shifted to higher wavelength (462 cm^{-1}) for 700°C compared with the 800°C (461 cm^{-1}) and 900°C (460 cm^{-1}) samples. The peaks at 432 cm^{-1} and 439 cm^{-1} combined into a single peak (435 cm^{-1}) after further oxidation. However, the peak intensity decreased at 800°C, almost disappearing at 900°C. The peak at 418 cm^{-1} for the 700°C sample separated into two, but having decreased intensity for the 800°C and 900°C samples. The peak at 409 cm^{-1} shifted to 403 cm^{-1}, 410 cm^{-1}, and 407 cm^{-1} for the 700°C, 800°C, and 900°C samples, respectively. It can be inferred that such broadening and shifting of the peaks may be due to formation or growth of an interfacial layer.

Fig. 6. Transmittance spectra of samples oxidized at various temperatures (600°C to 900°C).

Fig. 7. Raman spectra of samples oxidized at various temperatures (600°C to 900°C).

Fig. 8. Intensities of semipolycrystalline IL signal at 245 cm^{-1} and 477 cm^{-1} as function of oxidation temperature (600°C to 900°C).

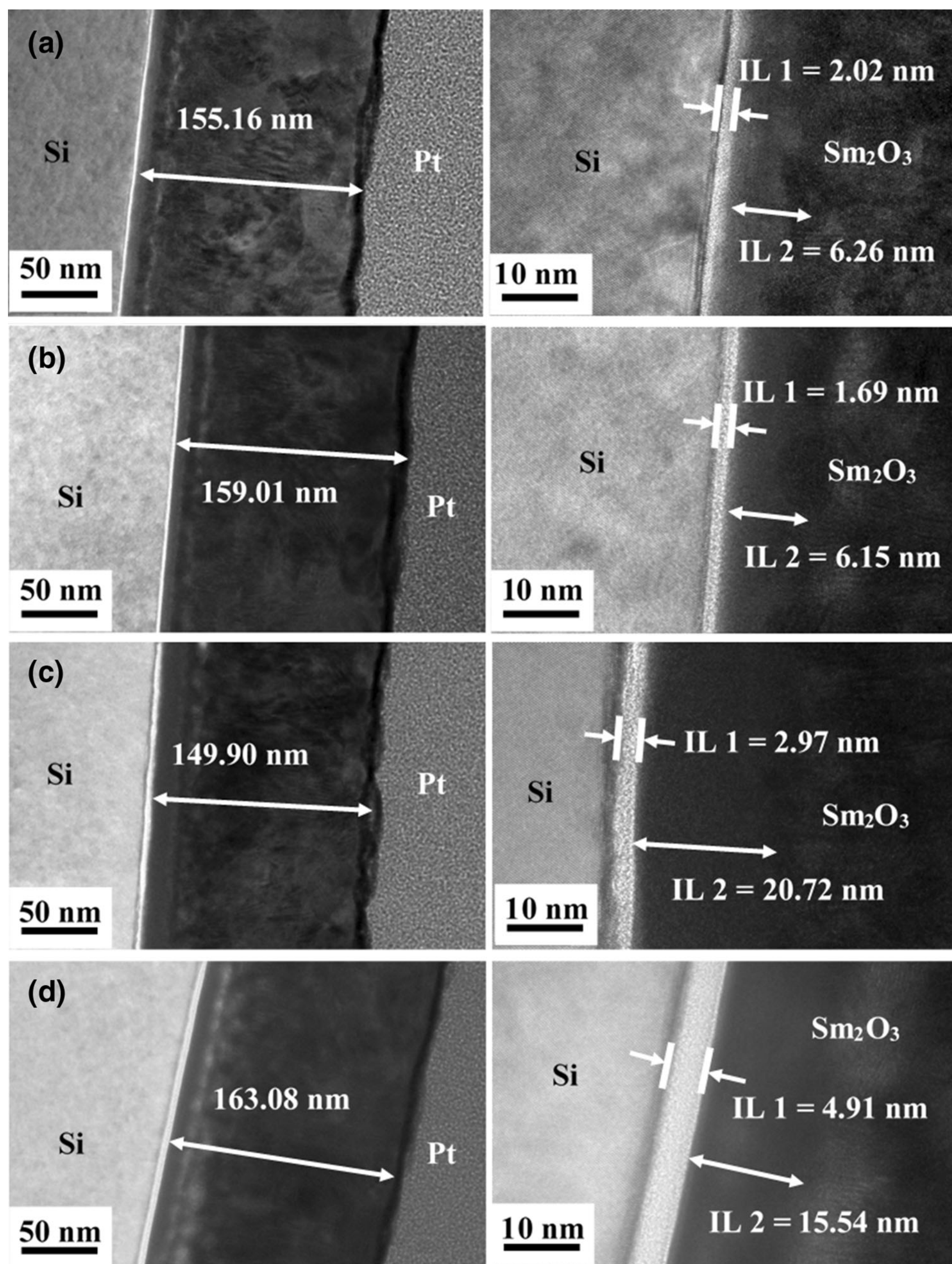

Fig. 9. Cross-sectional TEM images of samples oxidized at various temperatures: (a) 600°C, (b) 700°C, (c) 800°C, and (d) 900°C. A magnification of each image is shown on the bottom-left side.

The Raman results for all the oxidized samples are shown in Fig. 7. The peak at 520 cm^{-1} is assigned to the silicon substrate.[12] The peaks at 111 cm^{-1},[49] 120 cm^{-1},[49] 145 cm^{-1},[49] 168 cm^{-1},[49,50] 177 cm^{-1},[49] 238 cm^{-1},[49–51] and 408 cm^{-1}[49–51] are identified as corresponding to Sm_2O_3. The intensity of the unknown peaks at 245 cm^{-1} and 477 cm^{-1} increased as the oxidation temperature was increased owing to improved crystallinity (Fig. 8). Since they belong to neither Sm_2O_3 nor Si, they are inferred to correspond to a semipolycrystalline interfacial layer, as inferred from the results of XRD and FTIR analyses.

Figure 9 shows cross-sectional HRTEM images of samples oxidized at different temperatures (600°C to 700°C). Magnified images of each oxidized samples are shown on the bottom left-hand side. It is observed that the oxide/semiconductor structure consists of four layers, i.e., Si substrate, interfacial layer-1 (IL-1), IL-2, and Sm_2O_3 layer. The total oxide layer thickness for 600°C, 700°C, 800°C, and 900°C was 155.16 nm, 159.01 nm,

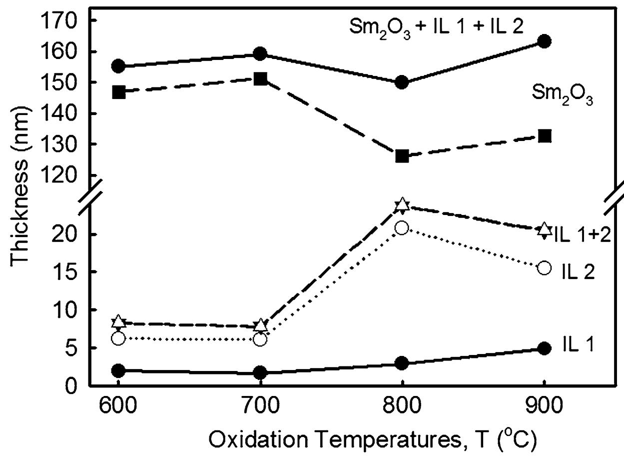

Fig. 10. IL-1, IL-2, IL-1 + 2, Sm_2O_3, and total thickness as functions of oxidation temperature (600°C to 900°C).

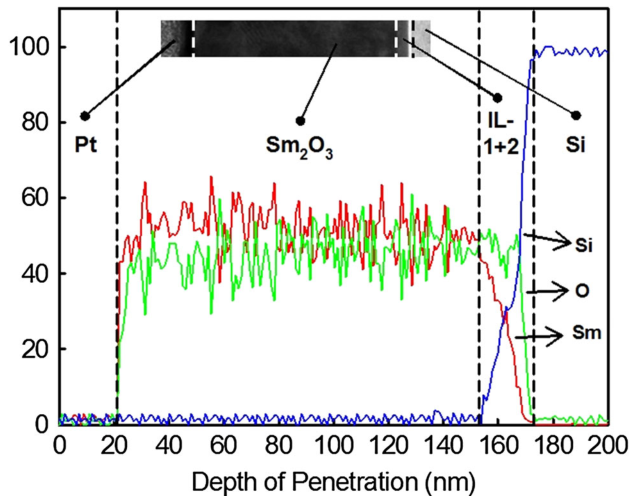

Fig. 11. EDX compositional analysis of Sm_2O_3 and Si elements for oxidized samples.

149.9 nm, and 163.08 nm, respectively. The IL-1 thickness for 600°C, 700°C, 800°C, and 900°C was 2.02 nm, 1.69 nm, 2.97 nm, and 4.91 nm, respectively. The IL-2 thickness for 600°C, 700°C, 800°C, and 900°C was 6.26 nm, 6.15 nm, 20.72 nm, and 15.54 nm, respectively. Sm_2O_3 lattice fringes can be clearly seen with interplanar spacing (d) of 0.194 nm to 0.258 nm as measured from the images, in agreement with the average d value (0.228 nm) of Sm_2O_3 from ICSD data. Polycrystalline structure of Sm_2O_3 and amorphous structure of IL-1 were revealed for all investigated samples. However, IL-2 exhibited semipolycrystalline nature for all samples. Hence, it is inferred that the two unknown peaks in Raman analysis are due to the presence of semipolycrystalline interfacial layers. The total thickness of the 800°C sample was the least (Fig. 10). However, its interfacial layer (IL-1 + 2) was the thickest among the samples. For oxidation temperature of 700°C, both interfacial layers were the thinnest, while the Sm_2O_3 layer was the thickest among the samples (Fig. 10). The total thickness of interfacial layer increased dramatically at oxidation temperature of 800°C and 900°C. This is because oxygen atoms actively diffused to the Sm_2O_3/Si interface from crystal defects and nonstoichiometric compounds when the oxidation temperature was increased.[22]

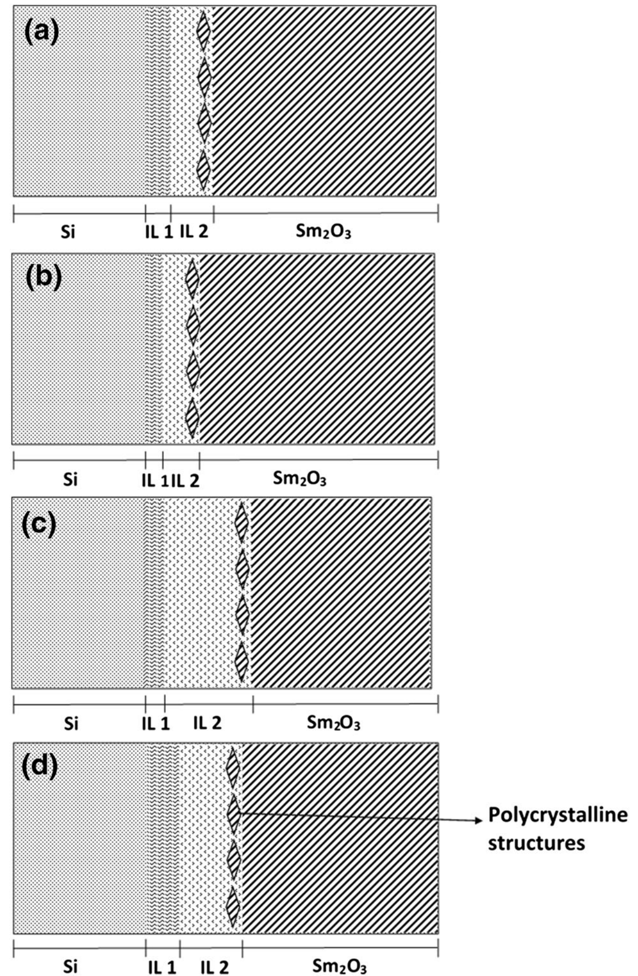

Fig. 12. Models of layer distributions for different oxidation temperatures: (a) 600°C, (b) 700°C, (c) 800°C, and (d) 900°C.

EDX line-scan compositional analysis revealed that not only an Sm_2O_3 layer is formed but also an Sm-O-Si interfacial layer between the Sm_2O_3 layer and Si substrate (Fig. 11). Based on the EDX, XRD, FTIR, and Raman results, a physical model is proposed in Fig. 12. At 600°C, oxygen (O) reacts with Sm to form Sm_2O_3. At the same time, Si also diffuses into Sm_2O_3 to form an interfacial layer ($Sm_xSi_yO_z$). As shown by EDX analysis, an Si-rich $Sm_xSi_yO_z$ layer (IL-1) is located near to the Si substrate, while an Sm-rich $Sm_xSi_yO_z$ layer (IL-2) is located near the Sm_2O_3. According to HRTEM, IL-2

exhibited semipolycrystalline structure, while IL-1 exhibited amorphous structure. Some polycrystalline structures could be observed in regions between IL-2 and Sm_2O_3. At 700°C, the growth rate of stable Sm_2O_3 was faster than for $Sm_xSi_yO_z$, so the thickest Sm_2O_3 layer formed with both ILs being the thinnest. However, an undesirable thick interfacial layer aggressively formed when the oxidation

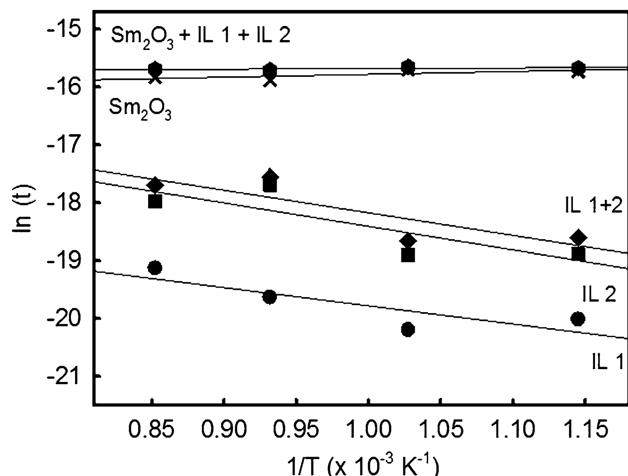

Fig. 13. Arrhenius plots of IL-1, IL-2, IL-1 + 2, Sm_2O_3, and total thickness in O ambient.

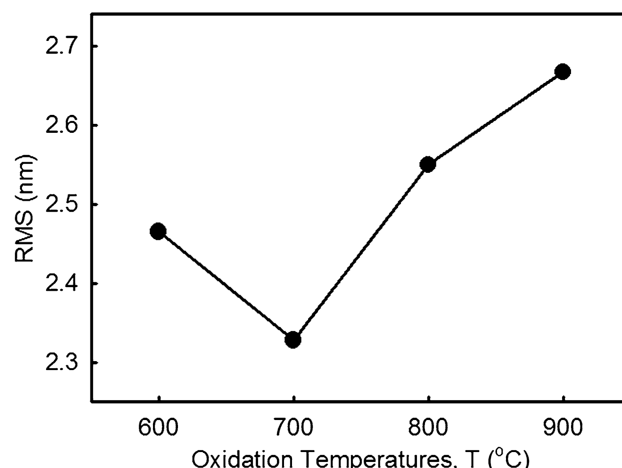

Fig. 15. RMS values of samples oxidized at various temperatures (600°C to 900°C).

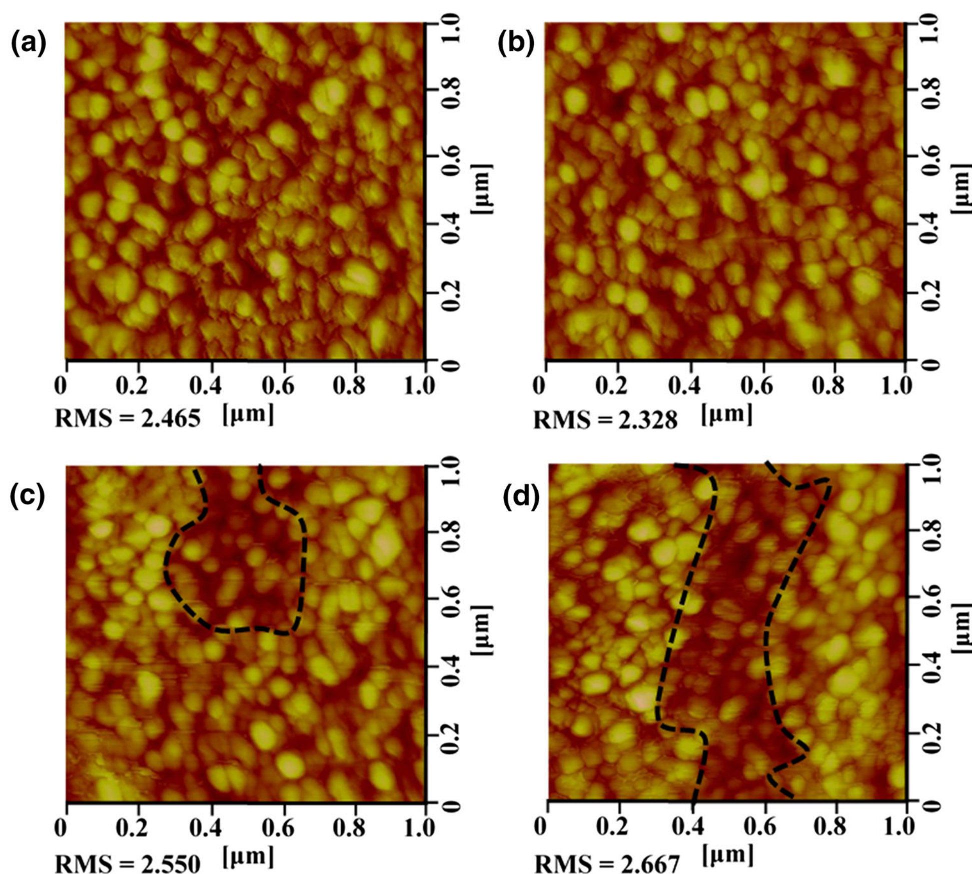

Fig. 14. Two-dimensional surface topography of samples oxidized at various temperatures: (a) 600°C, (b) 700°C, (c) 800°C, and (d) 900°C.

temperature was increased to 800°C and 900°C. The reaction between Sm_2O_3 and Si occurred rapidly to form thick $Sm_xSi_yO_z$ because of the higher activation energy under higher-temperature ambient.

Figure 13 shows the Arrhenius plot of IL-1, IL-2, IL-1 + 2, Sm_2O_3, and total (IL-1 + IL-2 + Sm_2O_3) growth in O ambient. The IL-1, IL-2, IL-1 + 2, Sm_2O_3, and total growth rates were identified to be governed by

$$t = t_0 \exp\left(\frac{-E_a}{kT}\right), \quad (6)$$

where E_a is the reaction activation energy, k is the Boltzmann constant, and t and t_0 are the final and initial thickness, respectively, of IL-1, IL-2, IL-1 + 2, Sm_2O_3, and all layers at given temperature T (K). The E_a values calculated for the IL-1, IL-2, IL-1 + 2, Sm_2O_3, and total growth rates were 2.7×10^{-4} eV, 3.5×10^{-4} eV, 3.4×10^{-4} eV, -4.3×10^{-5} eV, and -8.6×10^{-6} eV, respectively. Positive values of E_a indicate that the reaction rate will increase as the oxidation temperature is increased. This indicates that the thickness of the interfacial layers will increase as the oxidation temperature is increased. Negative values of E_a indicate that the reaction rate decreases or densification occurs as the oxidation temperature is increased. Moreover, the magnitude indicates the reaction tendency, with low magnitude indicating aggressive growth while large magnitude indicates slow growth.

Figure 14 shows the two-dimensional surface topography of the oxidized samples obtained by atomic force microscopy (AFM) over scanned areas of 1 μm × 1 μm. The surface roughness decreased when the oxidation temperature was increased from 600°C to 700°C, but increased again from 700°C to 900°C (Fig. 15). This may be due to consolidation of grains, with grain formation being favored at 700°C but grain clustering (dotted line in Fig. 14c, d) starting at higher temperatures (800°C and 900°C).[22,23] A similar phenomenon occurred in previous work where it was reported that RMS values decreased then increased again as the annealing temperature was increased.[23]

Figure 16 shows the leakage current density–electric field (J–E) characteristics for the investigated samples. The current–voltage (I–V) measurement results were transformed to a J–E plot. The E value was obtained from

$$E = \frac{(V_g - V_{fb})}{t_{ox}} \quad (7)$$

where V_g is the gate voltage, V_{fb} is the flatband voltage and t_{ox} is the oxide thickness.

Two-step oxide breakdown was revealed in all the characterized MOS capacitors. This is due to premature breakdown at lower electrical field (E_S) of

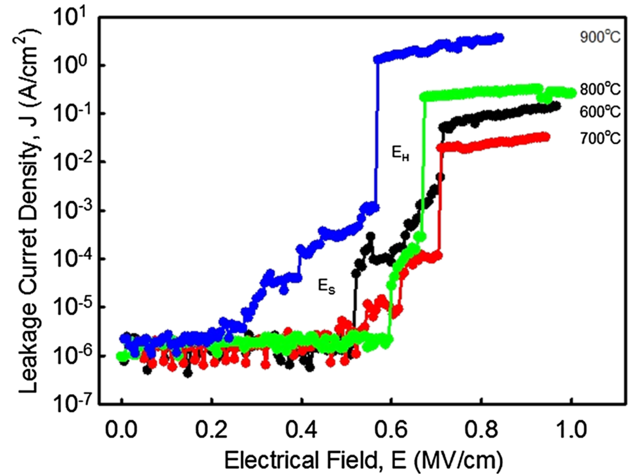

Fig. 16. J–E characteristics of samples oxidized at various temperatures (600°C to 900°C).

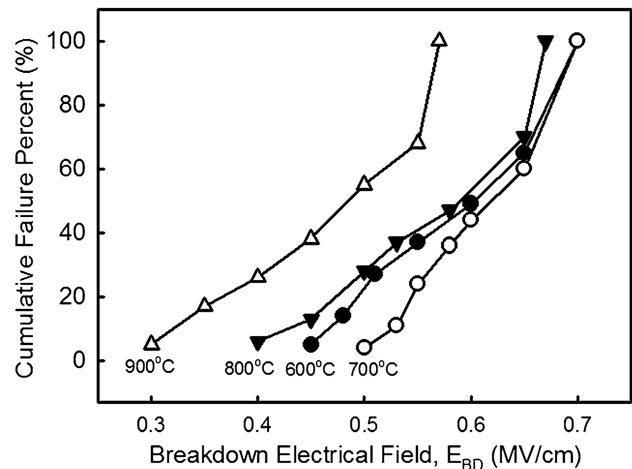

Fig. 17. Cumulative failure percentage of dielectric breakdown field (EBD) of samples oxidized at various temperatures (600°C to 900°C).

one layer (Sm_2O_3 or IL). Another layer will block the carriers until its electrical breakdown at higher electrical field (E_H). The instantaneous increment of leakage current density at E_S is relatively small, being defined as soft breakdown. For E_H, the instantaneous increment is larger, being defined as hard breakdown.

The samples oxidized at 600°C and 700°C showed almost the same E_H values. However, the J value was relatively lower for the sample oxidized at 700°C. The thickest IL in the sample oxidized at 900°C, as shown by TEM analysis, may degrade its electrical breakdown properties. Surface roughness may also be a factor affecting the electrical breakdown of the samples. The smoother samples (those oxidized at 600°C and 700°C) showed higher electrical breakdown fields compared with the relatively rougher samples (those oxidized at 800°C and 900°C). Rough and larger grains may lead to faster

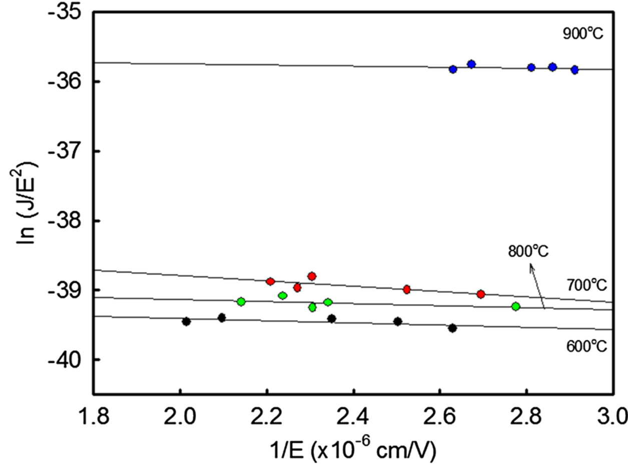

Fig. 18. FN tunneling linear regression plot of ln(J/E^2) versus $1/E$ for samples oxidized at various temperatures (600°C to 900°C).

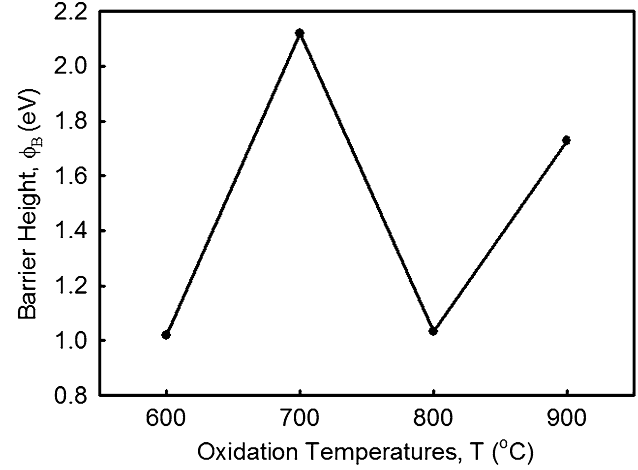

Fig. 19. Barrier height values as function of oxidation temperature (600°C to 900°C).

electrical breakdown compared with small and fine grain structure, because grain boundaries act as current transport paths. For smaller grain size, it is much more difficult for the current to cross thin films compared with larger grain size. Based on the J–E measurements, time-zero dielectric breakdown (TZBD) reliability tests were carried out at room temperature (25°C). The cumulative failure percentage of 100 capacitors is presented in Fig. 17. According to this plot, the sample oxidized at 700°C showed the best reliability.

The barrier height, $\O_B$ of the conduction-band edge between Si and the interfacial layer of the oxide was extracted from a Fowler–Nordheim (FN) tunneling model. FN tunneling (J_{FN}) refers to flow of electrons through a triangular potential barrier into the conduction band of an insulator, which can be defined as

$$J_{FN} = AE^2 \exp\left[\frac{-B}{E}\right], \tag{8}$$

where

$$A = \left[\frac{q^3}{8\pi h \Phi_B}\right]\left[\frac{m}{m_{ox}}\right], \tag{9}$$

$$B = \frac{8\pi\left(m_{ox}\Phi_B^3\right)^{1/2}}{3qh}, \tag{10}$$

where h is Planck's constant (4.135×10^{-15} eV s), m_{ox} is the effective electron mass in the oxidized layer, and m is the free electron mass. After replacing all constants, A and B can be expressed as

$$A = 1.54 \times 10^{-6}\left[\frac{m}{m_{ox}}\right][\Phi_B], \tag{11}$$

$$B = 6.83 \times 10^{7}\left[\frac{m_{ox}}{m}\right]\left[\Phi_B^3\right]^{1/2}. \tag{12}$$

Rearranging Eq. 8, one obtains

$$\ln\left[\frac{J}{E^2}\right] = -B\left[\frac{1}{E}\right] + \ln A. \tag{13}$$

Figure 18 shows a linear FN plot of $\ln(J/E^2)$ versus $1/E$. The gradient of the plot yields B, while the intercept yields A. To calculate $\O_B$, the effective mass of the high-κ oxide was assumed to be $0.3m$. The values of $\O_B$ range from 1.02 eV to 2.13 eV (Fig. 19). The sample oxidized at 700°C possessed the highest $\O_B$ value (2.13 eV).

CONCLUSIONS

Pure Sm metal layers sputtered on Si substrates were oxidized by a thermal oxidation process in oxygen ambient at various temperatures (600°C to 900°C) for 15 min. The existence of polycrystalline Sm_2O_3 and semipolycrystalline interfacial layers was confirmed by XRD, Raman, and EDX results, as also supported by FTIR results indicating broadening and/or shifting of Sm–O and Si–Si bonding peaks. Based on these results, a physical model is suggested. The Sm_2O_3 crystallite sizes calculated based on the W–H plot and Scherrer equation exhibited similar trends, increasing with oxidation temperature. The sample oxidized at 700°C had the thinnest interfacial layer and thickest Sm_2O_3 layer as measured from HRTEM images. It also had the smoothest surface, which gave the highest breakdown voltage field and lowest leakage current density compared with other samples with higher RMS thickness values. Moreover, its barrier height was also the highest among the investigated samples.

ACKNOWLEDGEMENTS

This project is funded by University of Malaya Research Grant (UMRG) Nos. RP013D-13AET and RP024A-13AET, Fundamental Research Grant Scheme (FRGS) Grant No. FP010-2013B, and Postgraduate Research Grant (PPP) No. PG048-2014A. The authors would also like to acknowledge the Faculty of Engineering and Faculty of Science, University of Malaya for providing the facilities and resources necessary for this research.

AUTHORS' CONTRIBUTIONS

K.H.G. was involved in experimental design, data acquisition, data interpretation and analysis, and drafting and revision of the manuscript. Y.H.W. and A.S.M.A.H. were involved in revising the manuscript critically for important intellectual content and gave final approval for the version submitted for publication.

CONFLICT OF INTEREST

The authors declare that they have no competing interests.

REFERENCES

1. J.B. Casady and R.W. Johnson, *Solid-State Electron.* 39, 1409 (1996).
2. A. Elford and P.A. Mawby, *Microelectron. J.* 30, 527 (1999).
3. P.R. Chalker, *Thin Solid Films* 343, 616 (1999).
4. Y.H. Wong and K.Y. Cheong, *J. Mater Sci-Mater. El.* 21, 980 (2010).
5. S.I. Ohmi, C. Kobayashi, K. Aizawa, S.I. Yamamoto, E. Tokumitsu, H. Ishiwara, and H. Iwai, in *31st European Solid-State Device Research Conference, ESSDERC* (2001) 235.
6. H.D. Kim and Y. Roh, *J. Korean Phys. Soc.* 49, 755 (2006).
7. V.V. Atuchin, V.N. Kruchinin, Y.H. Wong, and K.Y. Cheong, *Mater. Lett.* 105, 72 (2013).
8. Y.H. Wong and K.Y. Cheong, *Ceram. Int.* 39, 475 (2013).
9. Y.H. Wong and K.Y. Cheong, *Mater. Chem. Phys.* 136, 624 (2012).
10. Y.H. Wong and K.Y. Cheong, *J. Electrochem. Soc.* 159, 293 (2012).
11. Y.H. Wong and K.Y. Cheong, *Thin Solid Films* 520, 6822 (2012).
12. Y.H. Wong and K.Y. Cheong, *J. Alloy. Compd.* 509, 8728 (2011).
13. C.C. Chew, M.S. Gorji, K.H. Goh, C.G. Tan, S. Ramesh, and Y.H. Wong, *Appl. Phys. A-Mater.* 122, 66 (2016).
14. L. Shi, Y. Yuan, X.F. Liang, Y.D. Xia, J. Yin, and Z.G. Liu, *Appl. Surf. Sci.* 253, 3731 (2007).
15. J. Paivasaari, M. Putkonen, and L. Niinisto, *Thin Solid Films* 472, 275 (2005).
16. S.J. Jo, J.S. Ha, N.K. Park, D.K. Kang, and B.H. Kim, *Thin Solid Films* 513, 253 (2006).
17. G.D. Wilk, R.M. Wallace, and J.M. Anthony, *J. Appl. Phys.* 89, 5243 (2001).
18. M. Houssa, L. Pantisano, L.A. Ragnarsson, R. Degraeve, T. Schram, G. Pourtois, S. De Gendt, G. Groeseneken, and M.M. Heyns, *Mater. Sci. Eng. R* 51, 37 (2006).
19. T.M. Pan, W.T. Chang, and F.C. Chiu, *Appl. Surf. Sci.* 257, 3964 (2011).
20. W.C. Chin, K.Y. Cheong, and Z. Hassan, *Mater. Sci. Semicond. Proc.* 13, 303 (2010).
21. K.H. Goh, A.S.M.A. Haseeb, and Y.H. Wong, *Thin Solid Films* 606, 80 (2016).
22. T.M. Pan and C.C. Huang, *Appl. Surf. Sci.* 256, 7186 (2010).
23. F.H. Chen, M.N. Hung, J.F. Yang, S.Y. Kuo, J.L. Her, Y.H. Matsuda, and T.M. Pan, *J Phys. Chem. Solids* 74, 570 (2013).
24. C.H. Kao, H. Chen, K.S. Chen, C.Y. Huang, C.H. Huang, J.C. Ou, C.J. Lin, K.M. Lin, L.T. Kuo, in *10th IEEE International Conference on Solid-State and Integrated Circuit Technology Proceedings* (2010) p. 1425.
25. X.Y. Zhao, X.L. Wang, H. Lin, and Z.Q. Wang, *Phys. B* 403, 1787 (2008).
26. K. Shalini and S.A. Shivashankar, *Bull. Mater. Sci.* 28, 49 (2005).
27. C. Constantinescu, V. Ion, A.C. Galca, and M. Dinescu, *Thin Solid Films* 520, 6393 (2012).
28. A.A. Dakhel, *J. Alloy. Compd.* 365, 233 (2004).
29. V.A. Rozhkov, A.Y. Trusova, and I.G. Berezhnoy, *Thin Solid Films* 325, 151 (1998).
30. V.A. Rozhkov, V.P. Goncharov, A.Y. Trusova, in *Proceedings of the 1995 IEEE 5th International Conference on Conduction and Breakdown in Solid Dielectrics* (1995) p. 552.
31. S.Y. Huang, T.C. Chang, M.C. Chen, S.C. Chen, H.P. Lo, H.C. Huang, D.S. Gan, S.M. Sze, and M.J. Tsai, *Solid-State Electron.* 63, 189 (2011).
32. S. Kaya, E. Yilmaz, A. Kahraman, and H. Karacali, *Nucl. Instrum. Meth. B* 358, 188 (2015).
33. A.A. Dakhel, *J. Alloy. Compd.* 422, 1 (2006).
34. X.H. Cheng, D.P. Xu, Z.R. Song, D.W. He, Y.H. Yu, Q.T. Zhao, and D.S. Shen, *Appl. Surf. Sci.* 256, 921 (2009).
35. Y.P. Wu, S.F. Zhu, T.W. Liu, F.F. Li, Y.Z. Zhang, Y.C. Rao, and Y.B. Zhang, *Appl. Surf. Sci.* 307, 615 (2014).
36. M.A. Pampillon, P.C. Feijoo, E.S. Andres, M.L. Lucia, A. del Prado, and M. Toledano-Luque, *Microelectron. Eng.* 88, 2991 (2011).
37. K. Venkateswarlu, A.C. Bose, and N. Rameshbabu, *Phys. B* 405, 4256 (2010).
38. K. Santra, P. Chatterjee, and S.P. Sen Gupta. *Bull. Mater. Sci.* 25, 251 (2002).
39. S. Vives, E. Gaffet, and C. Meunier, *Mater. Sci. Eng. A-Str.* 366, 229 (2004).
40. V.D. Mote, Y. Purushotham, and B.N. Dole, *Cryst. Res. Technol.* 46, 705 (2011).
41. E.J. Mittemeijer and U. Welzel, *Z. Kristallogr.* 223, 552 (2008).
42. M. Herrmann, U. Forter-Barth, P.B. Kempa, and H. Krober, *Chem. Eng. Technol.* 32, 1067 (2009).
43. A.K. Zak, W.H.A. Majid, M.E. Abrishami, and R. Yousefi, *Solid State Sci.* 13, 251 (2011).
44. S. Miyazaki, *Appl. Surf. Sci.* 190, 66 (2002).
45. G.A.M. Hussein, D.J. Buttrey, P. DeSanto, A.A. Abd-Elgaber, H. Roshdy, and A.Y.Z. Myhoub, *Thermochim. Acta* 402, 27 (2003).
46. M.A. Ruiz-Gomez, C. Gomez-Solis, M.E. Zarazua-Morin, L.M. Tones-Martinez, I. Juarez-Ramirez, D. Sanchez-Martinez, and M.Z. Figueroa-Torres, *Ceram. Int.* 40, 1893 (2014).
47. H.M. Ismail, *Colloids Surfaces A* 97, 247 (1995).
48. E. Kusrini, R. Arbianti, N. Sofyan, M.A.A. Abdullah, and F. Andriani, *Spectrochim. Acta A* 120, 77 (2014).
49. S. Jiang, J. Liu, C.L. Lin, X.D. Li, and Y.C. Li, *J. Appl. Phys.* 113, 113502 (2013).
50. J. Mandal, B.J. Sarkar, A.K. Deb, and P.K. Chakrabarti, *J. Magn. Magn. Mater.* 371, 35 (2014).
51. T. Hongo, K.I. Kondo, K.G. Nakamura, and T. Atou, *J. Mater. Sci.* 42, 2582 (2007).
52. X.Y. Zhao, X.L. Wang, H. Lin, and Z.Q. Wang, *Mater. Sci. Semicond. Proc.* 33, 42 (2015).